

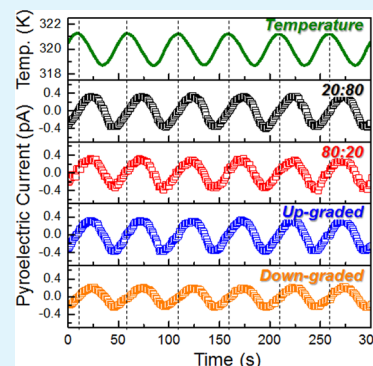
# Improved Pyroelectric Figures of Merit in Compositionally Graded $\text{PbZr}_{1-x}\text{Ti}_x\text{O}_3$ Thin Films

R. V. K. Mangalam, J. C. Agar, A. R. Damodaran, J. Karthik, and L. W. Martin\*

Department of Materials Science and Engineering and Materials Research Laboratory, University of Illinois, Urbana–Champaign, Urbana, Illinois 61801, United States

**ABSTRACT:** Pyroelectric materials have been widely used for a range of thermal-related applications including thermal imaging/sensing, waste heat energy conversion, and electron emission. In general, the figures of merit for applications of pyroelectric materials are proportional to the pyroelectric coefficient and inversely proportional to the dielectric permittivity. In this context, we explore single-layer and compositionally graded  $\text{PbZr}_{1-x}\text{Ti}_x\text{O}_3$  thin-film heterostructures as a way to independently engineer the pyroelectric coefficient and dielectric permittivity of materials and increase overall performance. Compositional gradients in thin films are found to produce large strain gradients which generate large built-in potentials in the films that can reduce the permittivity while maintaining large pyroelectric response. Routes to enhance the figures of merit of pyroelectric materials by 3–12 times are reported, and comparisons to standard materials are made.

**KEYWORDS:** ferroelectric, pyroelectric, permittivity, thin films, compositionally graded heterostructure,  $\text{PbZr}_{1-x}\text{Ti}_x\text{O}_3$



## INTRODUCTION

Ferroelectric materials have been utilized for a wide variety of applications including memories, actuators, infrared sensors, and electron emitters due to their susceptibility to electric field, stress, and temperature, respectively.<sup>1–4</sup> In general, the relative potential of a material for a given application can be described by an appropriate figure of merit (FoM). Focusing on ferroelectrics, one can generate figures of merit for memory, actuator, thermal, and other applications that are distinctly different. For the discussion here, we focus on thermal applications including infrared sensors and electron emitters where the FoM is  $\pi/C_p\epsilon_r\epsilon_0$  (where  $\pi$  is the pyroelectric coefficient and  $C_p$  is the heat capacity,  $\epsilon_r$  is the dielectric permittivity, and  $\epsilon_0$  is the permittivity of free space, henceforth referred to as  $\text{FoM}_{\text{IR}}$ )<sup>5,6</sup> and for pyroelectric energy conversion (PEC) systems where the figures of merit are  $\pi^2/\epsilon_r\epsilon_0$  or a closely related electrothermal coupling factor  $k^2 = \pi^2 T/C_p\epsilon_r\epsilon_0$  (where  $T$  is the temperature of operation, henceforth referred to as  $\text{FoM}_{\text{PEC}}$ ).<sup>7–9</sup> In the end, the definition of an appropriate FoM enables rapid assessment of what must be done to optimize or differentiate candidate ferroelectric materials for utilization in applications as diverse as memory, actuator/transducer, and thermal applications (i.e., thermal imaging/sensing,<sup>10</sup> waste heat energy conversion,<sup>11</sup> and electron emission<sup>12–14</sup>).

Upon closer inspection of the figures of merit for thermal applications a few terms are obviously important including the heat capacity, the pyroelectric coefficient, and the dielectric permittivity. Many of the highest performance pyroelectric materials are complex oxide systems with generic  $\text{ABO}_3$  chemistry. These materials generally possess heat capacity values that lie within a relatively small range (2–3.2 J/cm<sup>3</sup>

K),<sup>8,15</sup> making it difficult to tune these values in a technologically significant way. In turn, optimization of the pyroelectric performance of materials requires that one can independently enhance the pyroelectric coefficient (which describes the change in polarization of these materials with an applied temperature and dictates the quantity of charge that can be produced by a temperature stimulus) and suppress the dielectric permittivity (which describes the small-field, electric-field response of a material and is often used as a stand-in for electronic losses in a material in the FoM).<sup>16</sup> This optimization, however, is quite difficult in conventional materials where dielectric and pyroelectric responses are generally enhanced by the same generic features (i.e., proximity to structural phase transitions driven by chemistry, temperature, strain, etc.) making it difficult to decouple these effects. As a result, applications in the field of pyroelectrics have primarily focused on materials such as  $\text{LiNbO}_3$  and  $\text{LiTaO}_3$ ,<sup>5,6</sup> which possess moderate pyroelectric coefficients (−83 and −176  $\mu\text{C}/\text{m}^2\text{K}$ , respectively) but low room-temperature permittivity (31 and 54, respectively) and heat capacity values (2.8 and 3.16 J/cm<sup>3</sup>K, respectively).<sup>17</sup> In turn, for  $\text{LiNbO}_3$  ( $\text{LiTaO}_3$ ) the  $\text{FoM}_{\text{IR}} = 0.108 \text{ m}^2/\text{C}$  (0.116  $\text{m}^2/\text{C}$ ), and at 300 K the  $\text{FoM}_{\text{PEC}} = 0.0027$  (0.0062). Despite success in the application of such materials in macroscale devices, integration of these materials into advanced nanoelectronics and thin-film-based devices has been limited by the inability to produce films of these materials with the same properties and quality as single crystals.<sup>12</sup>

**Received:** September 26, 2013

**Accepted:** December 3, 2013

**Published:** December 3, 2013



In turn, the development of thin-film-based pyroelectrics with similar performance could enable utilization of these materials in new devices and presents additional routes by which to tune the responses using epitaxial strain, electrical boundary conditions, film thickness, artificial heterostructures, and more.<sup>18,19</sup> For example, epitaxial strain has been utilized to tune the pyroelectric coefficient and dielectric permittivity of  $\text{PbZr}_{0.2}\text{Ti}_{0.8}\text{O}_3$  thin films by controlling the  $90^\circ$  domain wall density.<sup>20,21</sup> Another area of study of particular interest for this work is that on compositionally graded ferroelectric thin films (including work on  $\text{PbZr}_{1-x}\text{Ti}_x\text{O}_3$  and other materials) which has revealed a range of novel phenomena such as built-in electric fields which give rise to self-poling,<sup>22</sup> shifted hysteresis loops,<sup>23,24</sup> enhanced pyroelectric susceptibilities,<sup>25–28</sup> and signatures of geometric frustration.<sup>29</sup> Such built-in biases are typically generated by inhomogeneous strains in multi-component superlattices<sup>30,31</sup> or by global composition gradients.<sup>22–27</sup> Extensive theoretical<sup>24,32–34</sup> and experimental<sup>22–27</sup> studies of compositionally graded ferroelectric heterostructures have proposed a range of intrinsic and extrinsic factors that could give rise to the built-in fields in these systems, but the work has been hampered by confusion as to the actual physical response. Early experiments on compositionally graded heterostructures reported a shift in the polarization (vertical) axis of the hysteresis loops, which was believed to be caused by gradients in the polarization within the material. The measured vertical offsets, however, were found to be explicitly dependent on the measurement circuit (i.e., the reference capacitor of the Sawyer–Tower circuit and the applied voltage),<sup>27,35</sup> to exhibit an exponential approach to a stable equilibrium after the application of an electric field, and to result in unphysical values of polarization ( $>250 \mu\text{C}/\text{cm}^2$  in compositionally graded  $\text{PbZr}_{1-x}\text{Ti}_x\text{O}_3$  films).<sup>23,36</sup> Later work<sup>37</sup> indicated that these observed shifts should, in fact, be along the voltage (horizontal) axis due to a built-in electric field but can manifest themselves as a polarization offset in a hysteresis measurement under certain measurement conditions. The observed horizontal shifts are, in turn, distinctly different from the shifts that arise from extrinsic effects such as asymmetric electrodes<sup>38</sup> or the inhomogeneous distribution of oxygen vacancies<sup>36</sup> in the ferroelectric.

Here we demonstrate the utilization of compositional gradients in thin-film heterostructures as a route to independently tune the pyroelectric and dielectric response of the canonical ferroelectric  $\text{PbZr}_{1-x}\text{Ti}_x\text{O}_3$ , thereby potentially enabling advanced thin-film thermal applications. Using such compositional gradients, we can engineer strain gradients to be  $>10^5 \text{ m}^{-1}$  (nearly 5–6 orders of magnitude larger than that achievable in bulk materials) which can, in turn, generate large built-in potentials<sup>39</sup> in the films that can effectively reduce the permittivity while maintaining large pyroelectric responses. As a result, we demonstrate figures of merit that are enhanced by 3–12 times as compared to single-layer  $\text{PbZr}_{1-x}\text{Ti}_x\text{O}_3$  films and by 1.1–4 times compared to standard materials such as  $\text{LiNbO}_3$  and  $\text{LiTaO}_3$ .

## EXPERIMENTAL METHODS

**Film Growth.** Single-layer and compositionally graded versions of 100 nm  $\text{PbZr}_{1-x}\text{Ti}_x\text{O}_3$  (PZT)/30 nm  $\text{SrRuO}_3/\text{GdScO}_3$  (110) heterostructures were grown using pulsed-laser deposition from  $\text{Pb}_{1.1}\text{Zr}_{0.2}\text{Ti}_{0.8}\text{O}_3$  and  $\text{Pb}_{1.1}\text{Zr}_{0.8}\text{Ti}_{0.2}\text{O}_3$  targets.<sup>39</sup> The laser fluence and repetition rate were maintained at  $1.9 \text{ J}/\text{cm}^2$  and 3 Hz for all PZT growths and  $1.8 \text{ J}/\text{cm}^2$  and 13 Hz for the growth of the  $\text{SrRuO}_3$ . The

bottom electrode  $\text{SrRuO}_3$  films were grown at  $630^\circ\text{C}$  in an oxygen pressure of 100 mTorr. The compositionally graded heterostructures were synthesized by continuously varying the composition from  $\text{PbZr}_{0.2}\text{Ti}_{0.8}\text{O}_3$  to  $\text{PbZr}_{0.8}\text{Ti}_{0.2}\text{O}_3$  and vice versa using a programmable target rotator (Neocera, LLC) that was synced with the excimer laser. The compositionally up-graded and down-graded heterostructures were grown at 600 and  $560^\circ\text{C}$ , respectively, at an oxygen pressure of 200 mTorr. For all the samples, films were cooled in an oxygen pressure of 700 Torr. Symmetric capacitor structures were fabricated by subsequent deposition of 80 nm  $\text{SrRuO}_3$  top electrodes defined using a  $\text{MgO}$  hard-mask process.<sup>40</sup> In this work, we focus on four sample variants: (1) single-layer  $\text{PbZr}_{0.2}\text{Ti}_{0.8}\text{O}_3$  (PZT20:80), (2) single-layer  $\text{PbZr}_{0.8}\text{Ti}_{0.2}\text{O}_3$  (PZT80:20), (3) compositionally up-graded PZT (which possesses a smooth transition between  $\text{PbZr}_{0.2}\text{Ti}_{0.8}\text{O}_3$  and  $\text{PbZr}_{0.8}\text{Ti}_{0.2}\text{O}_3$  upon transitioning from the substrate to film surface, up-graded), and (4) compositionally down-graded PZT (which possesses a smooth transition between  $\text{PbZr}_{0.8}\text{Ti}_{0.2}\text{O}_3$  and  $\text{PbZr}_{0.2}\text{Ti}_{0.8}\text{O}_3$  upon transitioning from the substrate to film surface, down-graded).

**Dielectric and Ferroelectric Properties.** The dielectric permittivity was extracted from the measured capacitance ( $C$ ) using  $C = ((\epsilon_0\epsilon_r A)/d)$  where  $A$  is the area of the capacitor and  $d$  is the thickness of the film. Prior to measurement, the films were poled with a negative bias for 0.1 ms, and films were measured at remanence. The dielectric permittivity as a function of frequency was measured with an ac excitation voltage of 8 mV (rms) (corresponding to a field of  $0.8 \text{ kV}/\text{cm}$ ) at various applied background dc electric fields ranging from 0 to  $-900 \text{ kV}/\text{cm}$ . Ferroelectric hysteresis loops were measured using a Radiant Multiferroics Tester as a function of frequency from 0.1 to 20 kHz.

**Pyroelectric Measurements.** The pyroelectric coefficient ( $\pi$ ) was measured using a phase-sensitive method.<sup>21,41</sup> A sinusoidal temperature oscillation of the form  $T = T_b + T_0 \sin(\omega t)$  with a background temperature of 320 K ( $T_b$ ) and 1.25 K ( $T_0$ ) amplitude was applied to the samples at 0.02 Hz ( $\omega = 0.125 \text{ rad/s}$ ). The pyroelectric current can be extracted as  $i_p = pAT_0\omega \cos(\omega t)$  as the pyroelectric current should be phase-shifted from the temperature oscillations by  $90^\circ$ . The measured pyroelectric currents were fitted to a sine function ( $i_0 \sin(\omega t + \phi)$ ) to extract the magnitude ( $i_0$ ) and phase ( $\phi$ ) of the pyroelectric current with respect to the temperature oscillation. The pyroelectric coefficient was then obtained by considering the out-of-phase component of the measured current as  $p = i_0 \sin(\phi)/AT_0\omega$ .

## RESULTS AND DISCUSSION

Previous studies<sup>39</sup> have revealed that single-layer PZT20:80 films are coherently strained to the substrate, while single-layer PZT80:20 films are partially relaxed. A similar asymmetry in strain relaxation is observed in the compositionally graded variants. Up-graded variants exhibit a nearly coherently strained tetragonal-like structure with lattice parameters  $a = 3.973 \text{ \AA}$  and  $c = 4.136 \text{ \AA}$ , while the down-graded variants exhibit complete strain relaxation and peaks for both the rhombohedral (PZT80:20) and tetragonal (PZT20:80) phases including evidence of in-plane  $a$  domain formation. This asymmetry is readily understood based on the fact that the lattice mismatch between PZT20:80 and PZT80:20 and the substrate is 0.8% (tensile) and  $-3.5\%$  (compressive), respectively. As a result, films with PZT80:20 near the substrate are much more susceptible to strain relaxation as compared to those with PZT20:80 near the substrate. Thus, in both the single-layer PZT80:20 and down-graded variants rapid strain relaxation occurs, and this presents the topmost Ti-rich phase with an effectively larger in-plane lattice parameter than the  $\text{GdScO}_3$  substrate which results in the formation of in-plane oriented  $a$  domains. When the Ti-rich material is grown at the substrate interface, as is the case of the up-graded heterostructures, the small lattice mismatch with the substrate is easily accom-

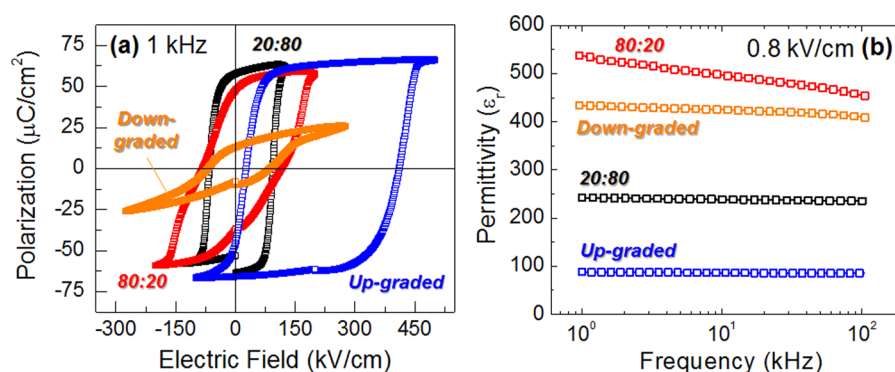


**Figure 1.** (a) Polarization–electric field hysteresis loops (measured at 1 kHz) and (b) dielectric permittivity ( $\epsilon_r$ ) as a function of frequency (measured at an ac excitation field of 0.8 kV/cm) for single-layer and compositionally graded heterostructures.

modated, and the subsequent Zr-rich material is presented with in-plane lattice parameters that are more favorable for generating a compressively strained variety of the Zr-rich phases. This has a direct analog to what has been observed in compositionally graded semiconductor heterostructures where large strains can be achieved across the film thickness because locally the lattice mismatch throughout the film is considerably smaller. These observations have been further confirmed via piezoresponse force microscopy studies of the domain structure. Both single-layer PZT20:80 and up-graded heterostructures reveal the presence of  $c/a/c/a$  domain structures. On the basis of the observed coherently strained nature of these films, a strain gradient of  $\sim 4 \times 10^5 \text{ m}^{-1}$  is expected in the up-graded heterostructures.

Subsequent studies of the dielectric and ferroelectric properties of these different heterostructure variants reveal dramatic differences (Figure 1). Recall that the capacitor structures used in these studies consist of symmetric top and bottom  $\text{SrRuO}_3$  electrodes. As expected for such symmetric capacitor structures, both the single-layer PZT20:80 and PZT80:20 heterostructures reveal ferroelectric hysteresis loops with large saturation and remanent polarization values that are symmetric about the zero bias (Figure 1a). The compositionally down-graded heterostructures also exhibit ferroelectric hysteresis loops that are symmetric about zero bias but with greatly diminished saturation and remanent polarization values (as a result of the presence of a large fraction of in-plane-oriented domains that are not switchable in the out-of-plane device structure). Compositionally up-graded heterostructures, on the other hand, reveal ferroelectric hysteresis loops that are shifted in the positive direction along the applied field axis due to the presence of a built-in potential.<sup>39,42</sup> Such built-in potentials arise due to the flexoelectric coupling between the strain gradient and the polarization in the out-of-plane direction.<sup>39,42–45</sup>

Beyond differences in the ferroelectric hysteresis loops in these single-layer and compositionally graded heterostructures, significant variation in the dielectric permittivity ( $\epsilon_r$ ) is observed (Figure 1b). The single-layer PZT80:20 and compositionally down-graded heterostructures exhibit relatively large dielectric permittivity due to their complex domain structures<sup>39</sup> which likely increase the extrinsic contribution from domain walls to the overall response. The single-layer PZT20:80 heterostructure reveals an intermediate dielectric permittivity consistent with the presence of  $c/a/c/a$  domain structures.<sup>20</sup> Finally, the compositionally up-graded heterostructures exhibit relatively low dielectric permittivity, con-

sistent with what is expected for monodomain PZT20:80, which can potentially be explained by the presence of the built-in potential in the films with large strain gradients.

To understand the importance of the built-in potential for the decrease in dielectric permittivity, we carried out capacitance measurement as a function of frequency between 1 and 200 kHz at different applied background dc electric fields. It has been demonstrated<sup>46</sup> that the applied background dc electric field can effectively suppress the extrinsic contributions from domain wall motion and allows for a quantitative measurement of the intrinsic response of the material—in other words, it provides a way to deconvolute intrinsic and extrinsic effects in materials. This is achieved by fitting the frequency dependence of the permittivity at each applied background dc electric field to the equation  $\epsilon = \epsilon_i - \alpha \log f$  and extracting the field dependence of the intercept ( $\epsilon_i$ ) and slope ( $\alpha$ ). From this data, one can extract the field at which extrinsic contributions are suppressed and the zero-field, intrinsic permittivity of a material. Here we report such background dc electric field measurements for both the single-layer PZT20:80 (which exhibit  $c/a/c/a$  domain structures and no built-in potential) (Figure 2a) and the compositionally up-graded (which exhibit  $c/a/c/a$  domain structures and a built-in potential) (Figure 2b) heterostructures. In general, the magnitude of the dielectric permittivity decreases as the applied background dc electric field is increased in magnitude from 0 to  $-900 \text{ kV}/\text{cm}$  on samples previously poled with large negative fields. The PZT20:80 heterostructures reveal  $\sim 60\%$  reduction in the dielectric permittivity with increasing applied background dc electric field (Figure 2a), whereas the compositionally up-graded heterostructures reveal only a  $\sim 36\%$  reduction (Figure 2b). Upon fitting the data, we extract values of  $\epsilon_i$  and  $\alpha$  as a function of applied background dc electric field.

For simplicity, we show the evolution of  $\epsilon_i$  only for the PZT20:80 (Figure 2c) and the compositionally up-graded heterostructures (Figure 2d). For both, the data reported are the average of measurements of three typical capacitors, and in general the response is very uniform across the capacitors (as evidenced by the small error bars). The data for the PZT20:80 heterostructures reveal two clear regimes (a low- and high-field regime) with a change in the trend around a field of magnitude 400–500 kV/cm. The low-field regime is generally thought to include information about both the intrinsic and extrinsic contributions to the permittivity, and the high-field regime is thought to be indicative of the response with the extrinsic contribution to permittivity suppressed. Linear fits to the low-field regime provide information about how the applied



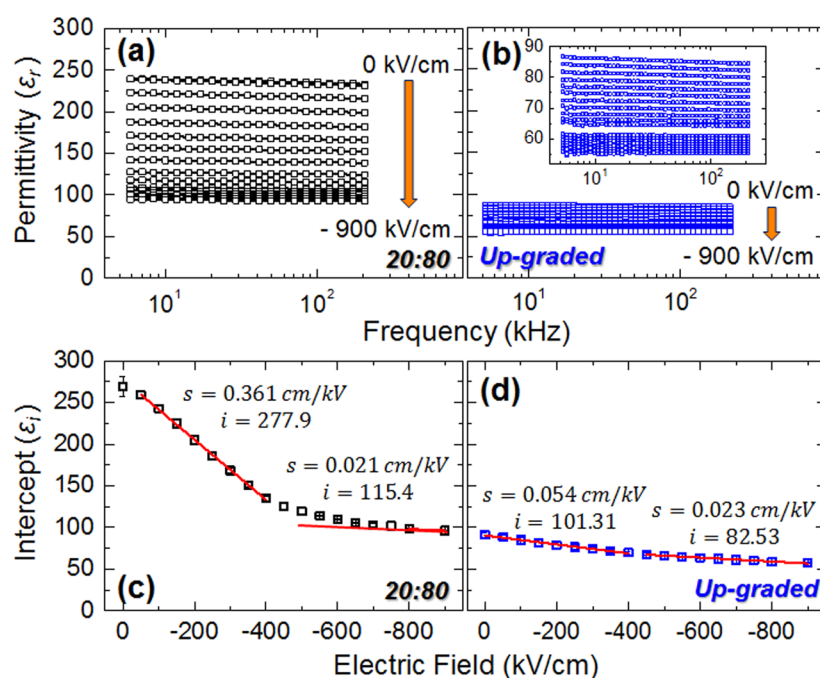


**Figure 2.** Dielectric permittivity is measured as a function of frequency at different applied background dc electric fields for (a) single-layer PZT20:80 and (b) compositionally up-graded heterostructures. The intercept ( $\epsilon_i$ ) obtained from a linear logarithmic fit of the dielectric permittivity–frequency data at different applied background dc electric fields is plotted as a function of the applied background dc electric fields for (c) single-layer PZT20:80 and (d) compositionally up-graded heterostructures.  $s$  and  $i$  are the slope and intercept values obtained from linear fits (red lines) of the  $\epsilon_i$  data.

background dc electric field suppresses the extrinsic response (slope,  $s$ ) and zero-field intrinsic–extrinsic permittivity (intercept,  $i$ ). Linear fits to the high-field regime provide information about how the applied background dc electric field suppresses the intrinsic response (slope,  $s$ ) and the zero-field intrinsic permittivity (intercept,  $i$ ). There is an order of magnitude decrease in the slope of the trends as one moves from the low- to high-field regimes (0.361 to 0.021 cm/kV, respectively) suggesting that the extrinsic response is much more susceptible to suppression with external fields. Additionally, the intercepts of the low- and high-field regimes are  $\sim 278$  (close to that studied in the dielectric measurements near zero-field, Figure 1b) and  $\sim 115$  (close to that expected for monodomain PZT20:80).<sup>47,48</sup> In other words,  $\sim 55\%$  of the zero-field, room-temperature permittivity arises from extrinsic contributions (consistent with prior observations of such materials).<sup>20</sup>

On the other hand, in compositionally up-graded heterostructures, which possess a built-in potential, only  $\sim 20\%$  of the zero-field, room-temperature permittivity arises from extrinsic contributions. Again, the background dc electric field measurements exhibit two response regimes, similar to the PZT20:80 heterostructures, across the field range studied herein with a change in the slope again occurring around a field of magnitude 400–500 kV/cm (Figure 2d). The slope of the low-field regime (0.054 cm/kV), however, is much smaller than that of the PZT20:80 heterostructure (0.361 cm/kV) suggesting that the extrinsic contribution is considerably smaller and that the presence of the built-in potential dramatically reduces the susceptibility of the domain walls to the ac excitation field. The slope of the high-field regime, on the other hand, is essentially the same (0.023 cm/kV) as that of the PZT20:80 heterostructures (0.021 cm/kV) suggesting that the fundamental response of the materials to the ac excitation field is

similar. The intercepts of the low- and high-field regimes for the compositionally up-graded heterostructures are  $\sim 101$  (close to that studied in the dielectric measurements near zero-field, Figure 1b) and  $\sim 83$  (accounting for the shift in the hysteresis loops). Again, these numbers are close to that expected for monodomain PZT20:80 but are less than that observed for the PZT20:80 heterostructures. We conjecture that the lower value observed for the extrapolated zero-field response in the compositionally up-graded heterostructure could be the result of the strain gradient in the film producing an inhomogeneous local field that can locally suppress the dielectric permittivity in regions where the field is highest. In turn, since the sample is then effectively a number of capacitors of different capacitance in series, the overall capacitance (and thus the permittivity) is dominated by the regions with the lowest response. Regardless, this study suggests that the presence of the built-in potential can greatly diminish the extrinsic contribution to permittivity. This potential effectively changes the energy landscape of the system, whereby it stiffens the domain walls against motion under the application of small ac excitation fields.

Having established the role of the built-in potential in driving changes in the ferroelectric and dielectric properties, we proceed to understand the effect of compositional grading on the evolution of pyroelectric response. The pyroelectric studies were completed with a sinusoidally varying temperature excitation centered about a background temperature of 320 K with a 1.25 K amplitude at 0.02 Hz (Figure 3a). The pyroelectric currents from the single-layer PZT20:80 and PZT80:20 heterostructures were probed for reference (Figure 3b and c, respectively). The magnitude of the pyroelectric current, and therefore the pyroelectric coefficient, from the PZT20:80 was greater than that of PZT80:20. Values of pyroelectric coefficients are given in Table 1. Likewise the compositionally up-graded and down-graded heterostructures

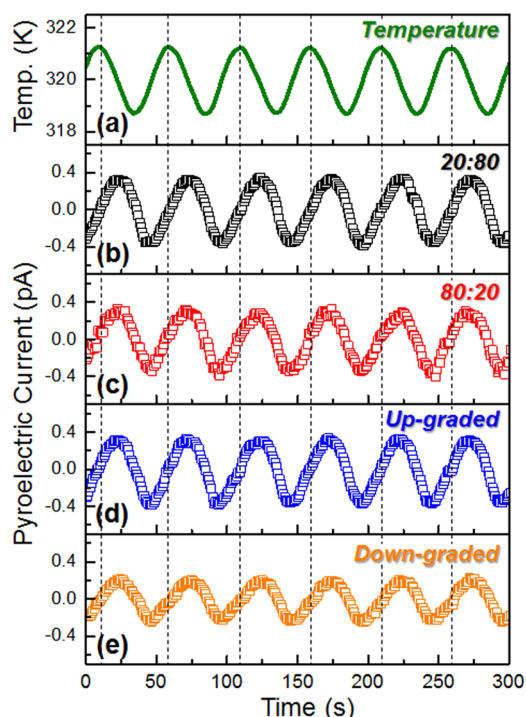


**Figure 3.** (a) Sinusoidal temperature variation applied to extract pyroelectric responses of (b) single-layer PZT20:80, (c) single-layer PZT80:20, (d) compositionally up-graded, and (e) compositionally down-graded heterostructures.

**Table 1.** Pyroelectric Coefficients ( $\pi$ ), Dielectric Permittivity ( $\epsilon_r$ ), Heat Capacity ( $C_p$ ), and the Thermal Imaging ( $\text{FoM}_{\text{IR}}$ ) and Pyroelectric Energy Conversion ( $\text{FoM}_{\text{PEC}}$ ) Figures of Merit for Single-Layer and Compositionally Graded Heterostructures and Classic Pyroelectric Materials

Heterostructure	$\pi$ ( $\mu\text{C}/\text{m}^2\text{K}$ )	$\epsilon_r$ (100 kHz)	$C_p$ (J/cm <sup>3</sup> K)	$\text{FoM}_{\text{IR}}$ ( $\times 10^{-2}$ , m <sup>2</sup> /C)	$\text{FoM}_{\text{PEC}}$ ( $\times 10^{-3}$ , 300K)
PbZr <sub>0.2</sub> Ti <sub>0.8</sub> O <sub>3</sub>	-300 ± 7	235	~3	4.81	4.33
PbZr <sub>0.8</sub> Ti <sub>0.2</sub> O <sub>3</sub>	-229 ± 11	453		1.90	1.31
Up-graded	-291 ± 4	85		12.9	11.3
Down-graded	-185 ± 13	409		1.70	0.95
LiNbO <sub>3</sub>	-83	31	2.8	10.8	2.69
LiTaO <sub>3</sub>	-176	54	3.2	11.6	6.15

were also probed (Figure 3d and e) and exhibited pyroelectric coefficients of a similar magnitude with the pyroelectric coefficient for the up-graded heterostructure being larger than that of the down-graded heterostructure (Table 1). The pyroelectric coefficients of the PZT20:80 and compositionally up-graded heterostructure are similar ( $-300$  and  $-291 \mu\text{C}/\text{m}^2\text{K}$ ), and more importantly, the presence of the built-in potential does not detrimentally influence the pyroelectric response of the material. The PZT80:20 exhibits a pyroelectric coefficient of  $-229 \mu\text{C}/\text{m}^2\text{K}$ , and the compositionally down-graded heterostructures exhibit a pyroelectric coefficient of  $-185 \mu\text{C}/\text{m}^2\text{K}$ . The observed differences are consistent with the ferroelectric domain structures observed in these heterostructures. The PZT20:80 and compositionally up-graded heterostructures exhibit  $c/a/c/a$  domain structures with a large volume of  $c$  domains (out-of-plane polarization) contributing to a relatively large pyroelectric current for a given temperature oscillation. On other hand, the PZT80:20 heterostructures exhibit a mosaic (rhombohedral) domain

structure, and the compositionally down-graded heterostructures have in-plane oriented tetragonal domains which contribute to the observation of a lower pyroelectric current compared to that of tetragonal  $c$  domains when measured along the  $[001]$  out-of-plane direction as completed herein.

The impact of these observations of dielectric and pyroelectric response can be summarized by revisiting the figures of merit described previously. Here we compare  $\text{FoM}_{\text{IR}}$  and  $\text{FoM}_{\text{PEC}}$  for the four heterostructure variants (Table 1). The heat capacity for the single-layer and compositionally graded PZT heterostructures is assumed to be  $\sim 3 \text{ J}/\text{cm}^3\text{K}$ , consistent with published reports,<sup>15</sup> and is assumed constant for all films. The limited usefulness of PZT materials for such pyroelectric applications is illustrated by the single-layer PZT20:80. Despite possessing a large pyroelectric coefficient, the correspondingly large dielectric constant leads to a rather pedestrian FoM. Among the four heterostructure variants, however, the compositionally up-graded heterostructure, as would be expected, reveals the largest figures of merit ( $\text{FoM}_{\text{IR}} = 0.129 \text{ m}^2/\text{C}$  and  $\text{FoM}_{\text{PEC}} = 0.0113$ ) due to the presence of a large pyroelectric coefficient and low dielectric permittivity. For both the PZT80:20 and compositionally down-graded heterostructures, the large dielectric permittivity (resulting from a complex domain structure) paired with rather smaller pyroelectric coefficients (resulting from the presence of some fraction of in-plane-oriented polarization) gives rise to low figures of merit. The large figures of merit for the compositionally up-graded heterostructure, however, are comparable and better than the traditionally utilized systems. For thermal imaging and pyroelectric energy conversion applications, respectively, the compositionally up-graded heterostructures are 1.1–1.2 times and 1.8–4.2 times larger than the figures of merit for ferroelectric single crystals of LiNbO<sub>3</sub> and LiTaO<sub>3</sub> (Table 1). These findings are important because for the first time it has been demonstrated that large pyroelectric figures of merit for a range of important and technologically relevant devices can be achieved in materials that can be readily generated as high-quality thin films. It should also be noted that the PZT family of materials has experienced considerable attention as both ferroelectric memories and for actuator/sensor applications, and thus existing infrastructure and knowledge bases exist on how to create these materials via scalable methodologies. Furthermore, the approach (i.e., the application of compositionally gradients) should be applicable to a wide range of materials and systems. The research on compositionally graded ferroelectric thin films has not been widely developed, and additional systems—potentially including Pb-free alternatives—may be developed. Additionally, the findings may have impacts beyond thermal applications to both tunable dielectrics, piezoelectrics, piezoelectric energy harvesting, and more. Overall, the approach illustrated herein suggests that compositionally grading materials may give researchers the ability to deterministically tune and control dielectric, ferroelectric, and pyroelectric properties individually—thereby decoupling these effects and allowing for exacting design of high-performance materials.

## CONCLUSION

In summary, we have observed that certain compositionally graded PZT heterostructures can be controlled to exhibit relatively low dielectric permittivity (as compared to single-layer and compositionally down-graded heterostructures) due to the presence of built-in potentials. The presence of the built-

in potential effectively diminishes the extrinsic contribution from the motion of domain walls to dielectric permittivity and renders the response commensurate with that expected from a single-crystal material. At the same time, the presence of the built-in potential does not impact the pyroelectric response, and large values of the pyroelectric coefficient are obtained. In the end, the combination of large pyroelectric coefficient and low dielectric permittivity in compositionally up-graded PZT heterostructure gives rise to large figures of merit, as large as 4.2-times larger for some cases, than those observed in single crystals of  $\text{LiNbO}_3$  and  $\text{LiTaO}_3$ . This exciting discovery could open up new materials and new small-scale applications within the realm of thermal effects including applications such as infrared sensors, pyroelectric electron emission systems, and pyroelectric energy conversion of waste heat.

## AUTHOR INFORMATION

### Corresponding Author

\*E-mail: lwmartin@illinois.edu.

### Author Contributions

The manuscript was written through contributions of all authors. All authors have given approval to the final version of the manuscript.

### Notes

The authors declare no competing financial interest.

## ACKNOWLEDGMENTS

R.V.K.M. and L.W.M. acknowledge the support of the Defense Advanced Research Projects Agency (DARPA) under grant number N66001-11-1-4195. J.C.A. and L.W.M. acknowledge support from the National Science Foundation under grant number DMR-1149062 and the Air Force Office of Scientific Research under grant AF FA 9550-11-1-0073. A.R.D. and L.W.M. acknowledge support from the Army Research Office under grant W911NF-10-1-0482. J. K. and L.W.M. acknowledge support from the Office of Naval Research under grant number N00014-10-1-0525. Experiments were carried out in part in the Materials Research Laboratory Central Facilities, University of Illinois, Urbana–Champaign.

## REFERENCES

- (1) Scott, J. F. *Science* **2007**, *315*, 954–959.
- (2) Baek, S. H.; Park, J.; Kim, D. M.; Aksyuk, V. A.; Das, R. R.; Bu, S. D.; Felker, D. A.; Lettieri, J.; Vaithyanathan, V.; Bharadwaja, S. S. N.; Bassiri-Gharb, N.; Chen, Y. B.; Sun, H. P.; Folkman, C. M.; Jang, H. W.; Kreft, D. J.; Streiffer, S. K.; Ramesh, R.; Pan, X. Q.; Trolier-McKinstry, S.; Schlom, D. G.; Rzhchowski, M. S.; Blick, R. H.; Eom, C. B. *Science* **2011**, *334*, 958–961.
- (3) Dawber, M.; Rabe, K. M.; Scott, J. F. *Rev. Mod. Phys.* **2005**, *77*, 1083–1130.
- (4) Setter, N.; Damjanovic, D.; Eng, L.; Fox, G.; Gevorgian, S.; Hong, S.; Kingon, A.; Kohlstedt, H.; Park, N. Y.; Stephenson, G. B.; Stolichnov, I.; Taganov, A. K.; Taylor, D. V.; Yamada, T.; Streiffer, S. *J. Appl. Phys.* **2006**, *100*, 051606.
- (5) Whatmore, R. W. *Rep. Prog. Phys.* **1986**, *49*, 1335–1386.
- (6) Shur, D.; Rosenman, G. *J. Appl. Phys.* **1996**, *80*, 3445–3450.
- (7) Sebald, G.; Seveyrat, L.; Guyomar, D.; Lebrun, L.; Guiffard, B.; Pruvost, S. *J. Appl. Phys.* **2006**, *100*, 124112.
- (8) Sebald, G.; Lefeuvre, E.; Guyomar, D. *IEEE Trans. Ultrason. Ferroelectr. Freq. Control* **2008**, *55*, 538–551.
- (9) Ashcon, N.; Laurent, P. *Smart Mater. Struct.* **2011**, *20*, 025012.
- (10) Lang, S. B. *Phys. Today* **2005**, *58*, 31–36.
- (11) Olsen, R. B.; Bruno, D. A.; Briscoe, J. M. *J. Appl. Phys.* **1985**, *58*, 4709–4716.
- (12) Rosenman, G.; Rez, I. *J. Appl. Phys.* **1993**, *73*, 1904–1908.
- (13) Fletcher, P. C.; Mangalam, R. V. K.; Martin, L. W.; King, W. P. *J. Vac. Sci. Technol. B* **2013**, *31*, 021805.
- (14) Fletcher, P. C.; Mangalam, R. V. K.; Martin, L. W.; King, W. P. *Appl. Phys. Lett.* **2013**, *102*, 192908.
- (15) Muralt, P. *Rep. Prog. Phys.* **2001**, *64*, 1339–1388.
- (16) Fang, J.; Frederich, H.; Pilon, L. *J. Heat Transfer* **2010**, *132*, 092701.
- (17) Beerman, H. P. *Infrared Phys.* **1975**, *15*, 225–231.
- (18) Schlom, D. G.; Chen, L.-Q.; Eom, C.-B.; Rabe, K. M.; Streiffer, S. K.; Triscone, J.-M. *Annu. Rev. Mater. Res.* **2007**, *37*, 589–626.
- (19) Martin, L. W.; Chu, Y. H.; Ramesh, R. *Mater. Sci. Eng., R* **2010**, *68*, 89–133.
- (20) Karthik, J.; Damodaran, A. R.; Martin, L. W. *Phys. Rev. Lett.* **2012**, *108*, 167601.
- (21) Karthik, J.; Agar, J. C.; Damodaran, A. R.; Martin, L. W. *Phys. Rev. Lett.* **2012**, *109*, 257602.
- (22) Mantese, J. V.; Schubring, N. W.; Micheli, A. L.; Catalan, A. B. *Appl. Phys. Lett.* **1995**, *67*, 721–723.
- (23) Brazier, M.; McElfresh, M.; Mansour, S. *Appl. Phys. Lett.* **1998**, *72*, 1121–1123.
- (24) Mantese, J. V.; Schubring, N. W.; Micheli, A. L.; Catalan, A. B.; Mohammed, M. S.; Naik, R.; Auner, G. W. *Appl. Phys. Lett.* **1997**, *71*, 2047–2049.
- (25) Schubring, N. W.; Mantese, J. W.; Micheli, A. L.; Catalan, A. B.; Lopez, R. L. *Phys. Rev. Lett.* **1992**, *68*, 1778–1781.
- (26) Jin, F.; Auner, G. W.; Naik, R.; Schubring, N. W.; Mantese, J. V.; Catalan, A. B.; Micheli, A. L. *Appl. Phys. Lett.* **1998**, *73*, 2838–2840.
- (27) Zhong, S.; Alpay, S. P.; Ban, Z.-G.; Mantese, J. V. *Appl. Phys. Lett.* **2005**, *86*, 092903.
- (28) Bao, D.; Yao, X.; Zhang, L. *Appl. Phys. Lett.* **2000**, *76*, 2779–2781.
- (29) Choudhury, N.; Walizer, L.; Lisenkov, S.; Bellaiche, L. *Nature* **2011**, *470*, 513–517.
- (30) Warusawithana, M. P.; Colla, E. V.; Eckstein, J. N.; Weissman, M. B. *Phys. Rev. Lett.* **2003**, *90*, 036802.
- (31) Callori, S. J.; Gabel, J.; Su, D.; Sinsheimer, J.; Fernandez-Serra, M. V.; Dawber, M. *Phys. Rev. Lett.* **2012**, *109*, 067601.
- (32) Pintilie, L.; Boerasu, I.; Gomes, M. J. M. *J. Appl. Phys.* **2003**, *93*, 9961–9967.
- (33) Alpay, S. P.; Ban, Z. G.; Mantese, J. V. *Appl. Phys. Lett.* **2003**, *82*, 1269–1271.
- (34) Ban, Z. G.; Alpay, S. P.; Mantese, J. V. *Phys. Rev. B* **2003**, *67*, 184104.
- (35) Ackay, G.; Zhong, S.; Allimi, B. S.; Alpay, S. P.; Mantese, J. V. *Appl. Phys. Lett.* **2007**, *91*, 012904.
- (36) Poullain, G.; Bouregba, R.; Vilquin, B.; Le Rhun, G.; Murray, H. *Appl. Phys. Lett.* **2002**, *81*, 5015–5017.
- (37) Brazier, M.; McElfresh, M.; Mansour, S. *Appl. Phys. Lett.* **1999**, *74*, 299–301.
- (38) Chan, H. K.; Lam, C. H.; Shin, F. G. *J. Appl. Phys.* **2004**, *95*, 2665–2671.
- (39) Mangalam, R. V. K.; Karthik, J.; Damodaran, A. R.; Agar, J. C.; Martin, L. W. *Adv. Mater.* **2013**, *25*, 1761–1767.
- (40) Karthik, J.; Damodaran, A. R.; Martin, L. W. *Adv. Mater.* **2012**, *24*, 1610–1615.
- (41) Bhatia, B.; Karthik, J.; Tong, T.; Cahill, D. G.; Martin, L. W.; King, W. P. *J. Appl. Phys.* **2012**, *112*, 104106.
- (42) Karthik, J.; Mangalam, R. V. K.; Agar, J. C.; Martin, L. W. *Phys. Rev. B* **2013**, *87*, 024111.
- (43) Pálóvá, L.; Chandra, P.; Rabe, K. M. *Phys. Rev. B* **2007**, *76*, 014112.
- (44) Catalan, G.; Sinnamon, L. J.; Gregg, J. M. *J. Phys.: Condens. Matter* **2004**, *16*, 2253–2264.
- (45) Catalan, G.; Noheda, B.; McAneney, J.; Sinnamon, L. J.; Gregg, J. M. *Phys. Rev. B* **2005**, *72*, 020102.
- (46) Narayanan, M.; Tong, S.; Liu, S.; Ma, B.; Balachandran, U. *Appl. Phys. Lett.* **2013**, *102*, 062906.

- (47) Vrejoiu, I.; Le Rhun, G.; Pintilie, L.; Hesse, D.; Alexe, M.; Gösele, U. *Adv. Mater.* **2006**, *18*, 1657–1661.
- (48) Haun, M. J.; Furman, E.; Jang, S. J.; Cross, L. E. *Ferroelectrics* **1989**, *99*, 63–86.